



## Investigating Cr dealloying and Li ingress in Ni-Mo-Cr alloys with different Mo/Cr ratio exposed to FLiNaK salt

Rumu H. Banerjee <sup>a,\*</sup>, Vishal Singh <sup>a,b</sup>, P. Chakraborty <sup>a</sup>, V. Karki <sup>c</sup>, G. Abraham <sup>d</sup>, R. Tewari <sup>a,b</sup>

<sup>a</sup> Materials Science Division, Bhabha Atomic Research Centre, Trombay, Mumbai 400 085, India

<sup>b</sup> Homi Bhabha National Institute, Trombay, Mumbai 400 094, India

<sup>c</sup> Fuel Chemistry Division, Bhabha Atomic Research Centre, Trombay, Mumbai 400 085, India

<sup>d</sup> Materials Processing and Corrosion Engineering Division, Bhabha Atomic Research Centre, Trombay, Mumbai 400 085, India

### ARTICLE INFO

#### Keywords:

Ni-Mo-Cr alloys  
Molten salt reactors (MSR)  
Cr diffusion  
FLiNaK salt

### ABSTRACT

Ni-Mo-Cr alloys (Hastelloy N and Hastelloy X) having different Mo/Cr ratio were exposed to FLiNaK salt at 973 K for 72 h in an in-house developed static corrosion test facility. Though both the alloys showed non-uniform attack and selective Cr dealloying, Hastelloy X showed enhanced localized corrosion owing to lower Mo/Cr ratio and pre-existing carbides. The carbides act as cathode in the alloy/precipitate micro-galvanic couple thereby accelerating the corrosion in the adjacent alloy surface. Furthermore, Li ingress into these alloys during corrosion was observed for the first time and in case of Hastelloy X, Li was found to form  $\text{Li}_2\text{CrO}_4$ .

### 1. Introduction

Molten salt reactors (MSR) are envisaged as one of the reactor classes to be developed under Generation IV reactor initiative [1,2], a promising technology towards clean and sustainable energy. These reactors offer several advantages over the conventional pressurized heavy water reactors in terms of (i) enhanced passive safety due to the absence of any core melt down possibility, (ii) strong negative temperature feedback due to larger thermal expansion (Nuclear Doppler effect) of the fluid fuel and increasing thermal conductivity with temperature ( $\sim 0.8 \text{ Wm}^{-1}\text{K}^{-1}$  at 1000 °C) enabling faster decay heat removal leading to increased inherent nuclear safety, (iii) higher burn up and higher operating temperatures resulting in higher efficiency, (iv) operation at ambient pressure (v) lower concentration of minor actinides generation with Th-cycle [1–3], to name a few. India too has been aggressively pursuing this technology mainly with the objective of online reprocessing to separate  $^{233}\text{Pa}$  thereby achieving  $^{233}\text{U}$  production [4] for the use in third stage of the three-stage nuclear program and the design of a prototype Indian Molten salt breeder reactor has been conceptualized [5,6].

In MSR, the major factors limiting the service life of the reactor are radiation stability as well as chemical compatibility of the structural materials with fluoride based molten fuel /coolant salt [7–9] and the fission products [10–12] that are generated during the course of reactor operation. The primary structural material considered for MSR

applications are Ni-Mo-Cr based alloys [1–3,13–16], namely Hastelloy N which was developed by ORNL during the initial studies on MSR. These solid-solution strengthened fcc alloys containing Cr and Mo offer high temperature stability combined with good resistance against corrosive attack by fluoride melt [3,14–18]. With the resurgence of interest in MSR, the attention on the development of different variants of the Ni-Cr-Mo based alloys has resurfaced [16–19]. The various candidate alloys proposed for different types of molten salt reactors are summarized in Table 1.

Similarly, the screening criteria for selecting secondary coolant salt require that the salt should (i) have high temperature chemical stability, (ii) be non-volatile and (iii) be compatible with high-temperature alloys, graphite, and ceramics [1–4]. These three basic requirements are fulfilled by (a) fluoride salts (b) alkali fluoroborates and (c) chloride salts [1–4,20]. Of these, a fluoride salt having eutectic composition as 46.5 mol% LiF- 11.5 mol% NaF- 42 mol% KF salt (FLiNaK salt) has emerged as the most promising candidate salt [20] owing to its excellent heat capacity, higher thermal conductivity, low vapour pressure, viscosity comparable to water and good compatibility with structural material [20]. The microstructural evolution in Hastelloy N upon exposure to FLiNaK salt with and without impurity additions [7,8,14–17,21–26] have been extensively investigated mainly in the context of Cr depletion but the phenomenon remains far from being completely understood.

It is accepted that the molten salt corrosion (MSC) of an alloy

\* Corresponding author.

E-mail address: [rumuhalder24feb@gmail.com](mailto:rumuhalder24feb@gmail.com) (R.H. Banerjee).

**Table 1**

Nominal compositions of candidate Ni-based alloys considered for use in MSR [6,7].

Alloy	Composition (wt%)					
	Mo	Cr	Fe	Mn	C	Ni
Hastelloy N	15.7	7.1	3.7	0.6	< 0.05	Balance
GH3535	17.1	7.0	4.0	0.8	< 0.02	Balance
MONICR	17.4	6.8	0.7	0.06	< 0.002	Balance
Nb-Modified	11–13	6–8	0.1	0.15–0.25	0.05	Balance
Hastelloy N					Nb:1–2	
HN80MTY	13.2	6.81	0.15	< 0.1	0.025	Balance
					Al:1.12	

**Table 2**

Nominal composition of the alloys chosen for present study as measured by XRF and ICP-MS. The values given in the parenthesis denote the error in measurements.

Element (wt%) Alloy	Ni	Mo	Cr	Fe	Mn	W	Co
Hastelloy N	Balance	16 (0.5)	7(0.5)	4 (0.1)	0.5 (0.1)	634 ppm	< 3 ppm
Hastelloy X	Balance	8.7 (0.1)	21.4 (0.4)	18.2 (0.3)	0.97 (0.14)	0.51 (0.08)	1.0

proceeds via the formation and dissolution of corrosion products across the salt-alloy interface [21–27]. The rate of corrosion in this case is controlled by the diffusivity of alloying elements into the salt. In the case, when a pure salt in contact with the alloy, the alloy is corroded by the salt till an equilibrium is reached and the alloy does not corrode any further. However, in actual service conditions, the salt may contain impurities including oxidants, thermal gradients, salt flow rate, and galvanic coupling which will alter the reaction rate [17,22–26]. Numerous studies have been conducted over past fifty years on the chemical compatibility between the Ni-Mo-Cr based structural material and the molten salt mainly in the context of salt impurities [22–26], salt redox potential [28] and choice of crucible material for the test [29]. However, there remains a gap in understanding of the mechanism of molten salt induced attack on the alloy especially in terms of prior microstructure and presence of secondary phases in the alloy. The role of Mo/Cr content on the surface layer modification and variation in the severity of intergranular attack is not yet studied in depth but such an investigation is of prime importance especially for designing the reactor

components where the alloy composition is modified under the service conditions. Furthermore, as per the authors' knowledge no available literature on study of the ingress/migration of Li, K and Na in the alloy and their possible role in the corrosion process is available.

To address these gaps in literature, present investigation was carried out with the objective of elucidating the effect of Mo/Cr ratio on the initial microstructure of the Ni-Mo-Cr alloy. In addition, the role of prior microstructure and in-service generated secondary phases in these alloys on their compatibility with molten salt was expounded. The ingress of elements from the salt into the alloy has also been investigated and their possible role in the corrosion mechanism is briefly outlined.

## 2. Experimental methodology

### 2.1. Sample preparation

Alloy coupons of commercially available Hastelloy N and Hastelloy X (Table 2) were cut into the cuboidal shape of dimensions ~1 cm<sup>3</sup>. X-ray fluorescence (XRF) measurements were performed to determine the major constituent elements while Inductively coupled plasma-mass spectrometry (ICP-MS) was used to determine the impurity content such as W and Co. The nominal compositions of these alloys thus obtained are presented in Table 2. The Mo/Cr ratio for Hastelloy X and N are respectively 0.4 and 2.2. Before exposure to the FLiNaK salt, the alloy coupons were grounded with abrasive papers and subsequently polished to mirror finish using the standard metallographic techniques. This is essential for the removal of the initial non-uniformity in the alloy structure which may act as a site for localized corrosion.

### 2.2. Preparation of molten salt set up for interaction study

The salt ingredients used in the present study i.e. LiF, NaF and KF were of > 99.9% purity and were in dried and sealed condition before use. Before the preparation of salt mixture, weighted amounts of the individual salt powders (46.5 mol% LiF–11.5 mol.% NaF–42 mol% KF) were preheated at 473 K for 2 h under continuous flow of high purity argon gas to remove any traces of oxygen and moisture. After pre-heating, the salt mixture was later prepared by mixing the powders in eutectic composition and heating the mixture at 873 K in Ni crucible in an in-house developed static corrosion test facility (schematic shown in Fig. 1(a)). It may be noted that the heating was carried out under flowing argon atmosphere in steps of 473 K, where the salt was soaked for 2 h after every 473 K was reached. Later the salt was cooled and the melting point of the resultant mixture was measured through Differential

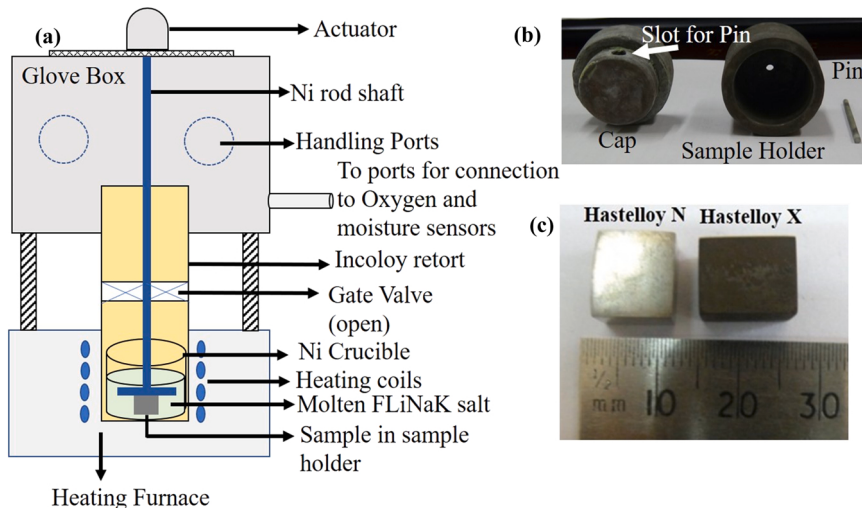


Fig. 1. (a) Schematic of the molten salt experiment bath, (b) Picture of the sample holder and (c) Alloy coupons after 72 h exposure to molten salt.

**Table 3**

Elemental analysis of FLiNaK salt before corrosion. The data for individual salts is as per the data sheets provided with the salts. The elemental concentration reported for the FLiNaK salt is determined by ICP-MS after melting of the salt from the weighted individual salts.

Maximum limit of impurities	LiF	NaF	KF
Sulphate ( $\text{SO}_4$ ) (%)	0.05	0.01	0.005
Iron (Fe) (%)	0.04	0.002	0.004
Water-insoluble matter (%)	–	6.01	0.005
Acidity (HF) (%)	–	0.05	0.05
Alkalinity ( $\text{NaOH} + \text{KOH}$ ) (%)	–	0.04	0.05
Chloride (Cl) (%)	–	0.003	0.005
Fluorosilicate ( $\text{SiF}_6$ ) (%)	–	0.1	0.05
Heavy metal (as Pb) (%)	–	0.001	0.001
<b>FLiNaK salt</b>			
Cr (ppm)	47		
Fe (ppm)	332.5		
Ni, Mo (ppm)	< 8		
Cu(ppm)	11.1		
Mn	0.4		
Al (%)	0.33		
Li (%)	9.49		
K (%)	13.82		
Na (%)	12.76		
F (%)	38.6		

Scanning Calorimetry (DSC) and was found to be 729 K (456 °C) which was very close to the melting point of FLiNaK (727 K or 454 °C). Afterwards, the salt was again heated to the operating temperature 973 K in a stepwise manner (1 h hold after every 473 K) before dipping on the alloy samples.

The Ni crucible used to melt the salt was not reduced using  $\text{H}_2$  gas. However, in order to reduce any oxygen impurities adhering to the Ni container, the first 500 gm of salt which was prepared in the Ni crucible was flushed off and discarded. The second batch of salt devoid of oxide impurities from Ni crucible which was prepared in the same way and used in the actual experiment. The various impurities in the salt quantified using mass spectrometry is presented in Table 3.

Once the salt is melted in Ni-crucibles, they are held at 973 K. The alloy samples placed in sample holders, which are also made up of Ni-based alloy, were then dipped into the molten salt. The holders containing alloy samples contain holes at the bottom which allow salt to enter into it (Fig. 1(b)) and the bath is then maintained at vacuum of  $10^{-6}$  mbar for the desired exposure duration of 72 h at 973 K (schematic in Fig. 1(a)). This procedure has been adopted preferentially over the hanging of samples so that all surfaces of the samples are exposed directly to molten salt. The holder is positioned at the centre of the Ni crucible and thus do not come in contact with the inner walls of the container after being dipped into the salt. The insertion and removal of the alloy coupons in sample holder is controlled by nickel rod connected to a linear actuator system. The corrosion experiment reported in the present study was carried out under inert atmosphere of high purity argon. The argon gas was passed through the oxygen and moisture traps attached to the facility, before pushing the same into the molten salt chamber. Flushing of the argon gas was conducted after every 3 – 4 h to release the accumulated vapours which are finally passed through a fluoride scrubber. Dedicated oxygen sensors attached to the inlet and outlet gas lines measured the oxygen content at every purge session. Throughout the experiment, the measured inlet and outlet oxygen content was found to be maintained at 5 ppm and 6 ppm respectively.

**Table 4**

Thickness and weight loss measurements.

Alloy	Weight loss $\Delta w$ (g)	Area A ( $\text{cm}^2$ )	Corrosion rate CR= $\Delta w/A.t$ ( $\mu\text{g}/\text{cm}^2/\text{h}$ )	Density of the alloy, $\rho$ ( $\text{g}/\text{cm}^3$ )	Thickness reduction rate = CR/ $\rho$ ( $\mu\text{m}/\text{h}$ )	Dissolution rate (m/s)
Hastelloy N	0.0051	4.8828	14.5	8.86	0.0163	$4.54 \times 10^{-12}$
Hastelloy X	0.07382	5.7132	179.4	8.22	0.208	$5.77 \times 10^{-6}$

The detailed description of the construction of the facility can be found in authors' previous work [19] and are not exclusively repeated here.

After completion of 72 h exposure, the alloys were cooled in the controlled environment outside the melt pool. The exposed alloy coupons were washed thoroughly with 1 mol/L solution of aluminium nitrate ( $\text{Al}(\text{NO}_3)_3$ ) [17,21,22] and afterwards cleaned ultrasonically using acetone to remove any residual solidified salt adhered to the exposed alloy surfaces. Fig. 1(c) shows the surface of exposed alloy coupons after cleaning. The mass of the alloy specimens before and after exposure to the salt is recorded. A blank cleaning test on unexposed sample was carried out to observe the effect of  $\text{Al}(\text{NO}_3)_3$  on weight loss/additional corrosion of the specimens. The solution was found to have negligible effect on the weight of the alloys. In addition, for comparison purpose, the alloys were aged at 973 K for 72 h and furnace cooled without any exposure to molten salt.

### 2.3. Characterization of the pre- and post-interacted alloy coupons

The morphology and microstructure of the exposed alloy coupons both along the surface as well as the cross-section, were characterized by a Field Emission - Scanning Electron Microscope (FE-SEM; Carl Zeiss Auriga Cross Beam) employing a focused electron beam accelerated at 5–20 keV. Both Secondary electron (SE) and back scattered electron (BSE) mode imaging was used to observe surface morphology and Z-contrast. The quantitative elemental analyses were carried out with energy dispersive spectroscopy (EDS). Micro-Raman spectroscopic measurements were recorded at room temperature for exposed and unexposed samples in the spectral range of 100–1000  $\text{cm}^{-1}$  using a Lab Ram HR 800 micro-laser Raman instrument having a focal length of 800 mm. The sample was excited by an air-cooled He-Ne laser having wavelength 633 nm operating at 17 mW. The laser beam had a diameter of  $\sim 1 \mu\text{m}$  and the spectral resolution of the instrument is  $1 \text{ cm}^{-1}$ .

A magnetic sector based Cameca SIMS-7 f secondary ion mass spectrometer (SIMS) instrument equipped with both oxygen ( $\text{O}_2^+$ ,  $\text{O}^-$ ) and cesium ( $\text{Cs}^+$ ) primary ion beams was used to investigate the depth profiles of salt elements diffused into the exposed alloy matrix [30]. Depth distribution analysis of these elements in samples were carried out using a  $\text{Cs}^+$  primary ion beam with beam current of 55 nA ( $\pm 1 \text{ nA}$ ) incident on the sample surface at an impact energy of 5 keV. Positive secondary ion detection mode has been utilized for the analysis. In order to remove the crater edge effects, primary ion beam was raster scanned over an area of  $250 \mu\text{m} \times 250 \mu\text{m}$ . The secondary ions were collected over an analysis region of  $\sim 150 \mu\text{m}$  in diameter at the centre of raster area by using a field aperture of 1800  $\mu\text{m}$  in diameter. All the measurements were performed at an UHV of  $\sim 4 \times 10^{-9}$  mbar with a mass resolution (m/dm) of  $\sim 400$  for removing the isobaric mass interferences caused by sample and residual gaseous species present in the analysis chamber.

## 3. Results

### 3.1. Dissolution rate for short term interaction

From the weight loss measurements of the alloys subsequent to exposure to FLiNaK salt, the corrosion rate and thickness reduction rates were estimated using the equations [19].

**Table 5**Chemical reactions possible at the alloy salt interface<sup>[17,21–23,26]</sup>.

Reactions	Remarks
$3NiF_2 + 2Cr^o \rightarrow 2CrF_3 + 3Ni^o$	Ni can deposit on alloy surface
$FeF_3 + 2Cr^o \rightarrow CrF_3 + Fe^o$	Fe can deposit on alloy surface
$2CrF_3 + Cr^o \rightarrow 3CrF_2$	Fluorides dissolve back into the salt
$Ni^o + 2F^- \rightarrow NiF_2$	
$Cr^o + 2F^- \rightarrow CrF_2$	
$Mo^o + 6F^- \rightarrow MoF_6$	
$2HF + Cr^o \rightarrow CrF_2 + H_2$	
$Na_2SO_4 + 2Cr^o \rightarrow S + Na_2O + 2Cr_2O_3$	
$2Cr_2O_3 - 3O^{2-} + 2Cr^{3+}$	$Cr^{3+}$ can oxidise the alloy

$$\text{Corrosion rate} \left( \frac{\mu\text{g}}{\text{cm}^2 \text{h}} \right) = \frac{\text{Weight loss(g)} \times 10^{-6}}{\text{Surface area exposed(cm}^2) \times \text{Duration of exposure(h)}} \quad (1)$$

$$\text{Thickness reduction rate} \left( \frac{\mu\text{m}}{\text{h}} \right) = \frac{\text{Corrosion rate} (\mu\text{g cm}^{-2} \text{h}^{-1}) \times 10^{-2}}{\text{Density of alloy(g.cm}^{-3})} \quad (2)$$

The corrosion rates and thickness reduction rates are enlisted in Table 4. The details of the mass loss for dissolution rate estimation is provided in Appendix. From the measurements, it is evident that Hastelloy X undergoes a weight loss which is almost ten times higher and the thickness reduction almost twenty times more than Hastelloy N.

To understand this phenomenon, it should be noted that during the initial periods of exposure, the intrinsic corrosion is driven by the fluorination of susceptible alloying elements as well as attack caused by impurities such as  $H_2O$  and HF. The tendency of fluoride formation by the alloying elements at 973 K is found to decrease in the following order [17,21–23].

$Cr > Fe > Ni > Mo$

Hence, the dissolution rates obtained in Hastelloy N and Hastelloy X could be directly correlated with Cr dissolution, since from free energy point of view formation of chromium fluorides is most favourable. The higher corrosion rate for Hastelloy X is mainly due to higher Cr content of Hastelloy X.

Comparison of the corrosion rates observed in the present case with

those reported by Olson et al. [30] for Alloy 617 reveal that Alloy 617 undergoes higher weight loss than of Hastelloy X in spite of having similar Cr content (20–24 wt%). This suggests that apart from Cr content, alloy chemistry and microstructure also play a critical role in determining the overall corrosion rate. Furthermore, the reported dissolution rate for Hastelloy N in FLiNaK salt containing moisture (3.19 wt%) at 973 K is  $785.2 \mu\text{g cm}^{-2} \text{h}^{-1}$  [22], approx. 4.4 higher than the rate evaluated in the present study. This shows that the moisture within the experimental set up during the exposure was well controlled. However, the minor oxidant impurities (Fe, N, sulphate, HF etc.) present in the salt can also play a major role in enhancing the Cr dissolution. The major fluorination reactions of the alloying elements are summarized in Table 5.

### 3.2. Effect of FLiNaK salt on surface morphology and alloy microstructure

#### 3.2.1. Surface morphology and elemental distribution

Representative microstructures of Hastelloy N and Hastelloy X in as-received condition are shown in Fig. 2(a) and (d) respectively. The as-received Hastelloy N comprises an austenitic matrix (fcc crystal structure) with numerous annealing twins and no precipitates or inclusions; while Hastelloy X shows a typical microstructure comprising an austenitic matrix and Mo rich precipitates mainly  $Mo_6C$  carbides (Fig. 2(d)). No Cr-rich phases were detected in the microstructure of Hastelloy X. Detailed microstructural analyses of Hastelloy X and Hastelloy N have been carried out elsewhere and are not repeated here [17,20,21,31–35]. Ageing at 973 K for 72 h results in the development of secondary carbide precipitates rich in Mo in both Hastelloy N and X (Fig. 2(b) and (e)). However, the fraction of Mo rich carbides is higher for Hastelloy X.

After exposure to molten salt, surfaces of both the specimens had lost the diamond mirror finish. The micrographs of the exposed alloy surface are presented in Fig. 2(c) and (f). The exposed surface of the alloys shows two distinct features, namely

- (i) Grain boundary attack with minimal attack on twin boundaries.
- (ii) Formation of pits within the grain matrix.

The extent of fluoride attack was found to be non-uniform with

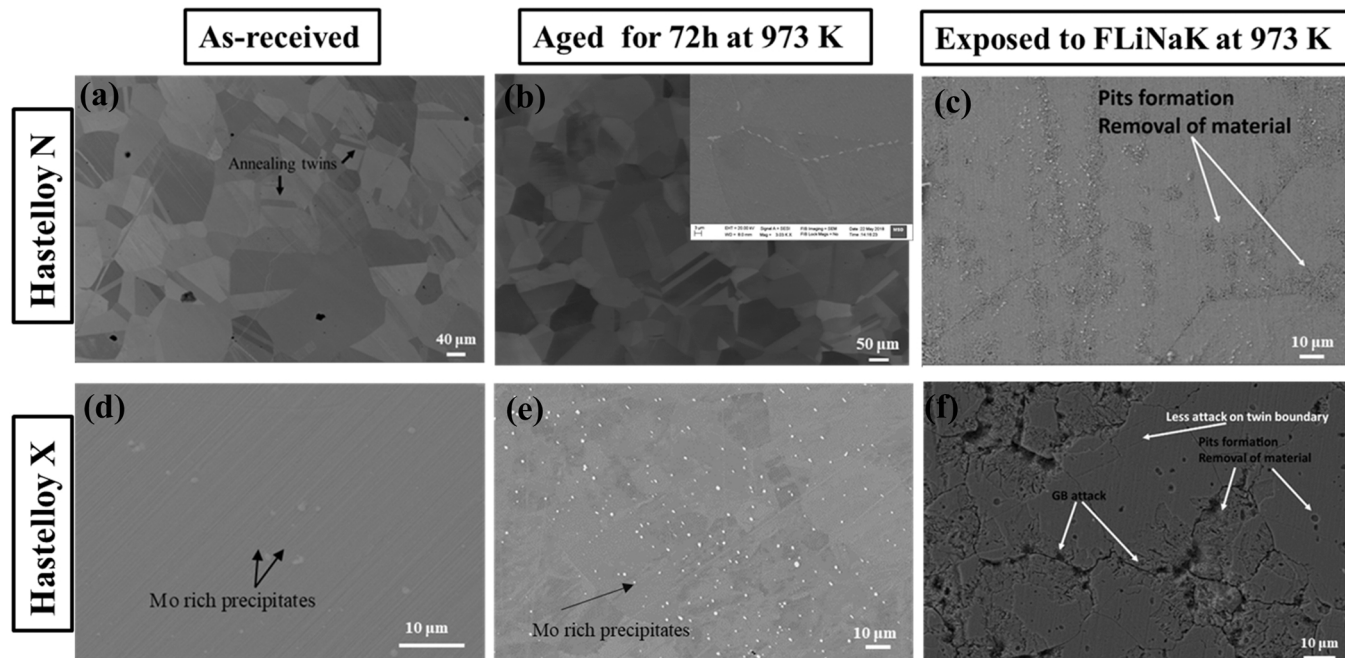
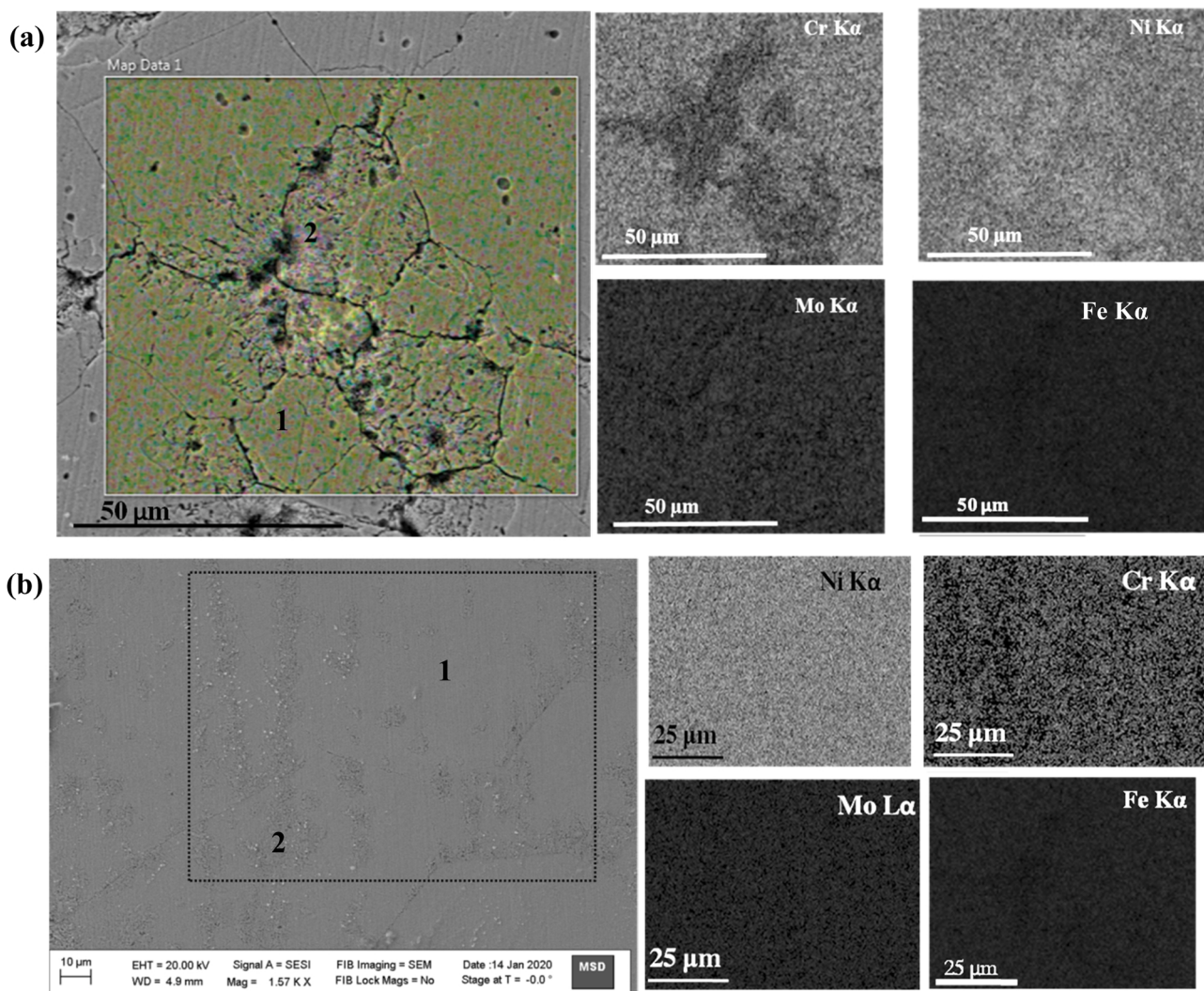


Fig. 2. Microstructure of Hastelloy N ((a)-(c)) and Hastelloy X ((d)-(f)) in as-received, aged (973 K for 72 h) and exposed to FLiNaK conditions, respectively.



**Fig. 3.** Elemental X-ray mapping of the corroded surface of (a) Hastelloy X and (b) Hastelloy N after 72 h exposure in molten salt environment.

**Table 6**

EDS point analysis carried out on the surface of exposed Hastelloy X coupon at point 1 and 2 marked in the image presented in Fig. 3(a), and the corresponding analyses for Hastelloy N coupon at position marked in Fig. 3(b).

Alloy	Element (wt%)→ Region of analysis↓	Ni	Cr	Mo	Fe
Hastelloy X	Surface region free from attack (point 1)	50.0 ± 0.3	21.7 ± 0.2	8.3 ± 0.2	17.4 ± 0.2
Hastelloy X	Surface region under fluoride attack (point 2)	65.3 ± 0.4	12.3 ± 0.2	8.5 ± 0.3	11.1 ± 0.2
Hastelloy N	Surface free from attack (point 1)	71.1 ± 0.3	6.7 ± 0.1	15.3 ± 0.3	3.7 ± 0.1
Hastelloy N	Surface under fluoride attack (point 2)	76.7 ± 0.3	3.3 ± 0.1	13.9 ± 0.3	3.9 ± 0.1

attack mainly concentrated along the grain boundaries showing accelerated attack as compared to the grain interiors which showed pit formation (Fig. 2(c), (f)). Such pit formation in grain matrix could be attributed to the dealloying of Cr and coalescence of the Cr vacancies [17,21–27] (irrespective of the presence of secondary phases). The regions adjacent to grain boundaries showed higher pit formation while the grain interiors showed number of pits to a lesser extent. Detailed elemental analyses using energy dispersive X-ray spectroscopy (EDS) and X-ray mapping (Fig. 3(a)) revealed that the pitted surface of Hastelloy X is depleted in Cr-content with negligible depletion in Ni and Mo as shown in Table 6. No attack was observed at the twin boundaries. Hastelloy N surface also exhibited grain boundary attack and pit formation (Fig. 3(b)).

The pit formation is associated with selective Cr depletion, as

indicated by the EDS point analyses (Table 6). The pit formation in grains is lesser in the case of Hastelloy N as compared to Hastelloy X. This could be attributed to the lower Cr content in Hastelloy N and also to the presence of higher fraction of Mo rich precipitates in Hastelloy that enhanced the number fraction of pits. Enhanced corrosion performance of the alloy when the carbide fraction is low has been observed by Muránsky et al. [8] where the MONICR alloy contained lower Mo-rich precipitates and hence showed lesser molten salt attack in comparison to GH3535 alloy.

### 3.2.2. Elemental depletion along the cross section

It is expected that the alloy will develop a Cr-depleted layer at the interface due to the outward diffusion and subsequent dissolution of Cr which grows deeper with time [27]. Fig. 4(a), (c) show the secondary

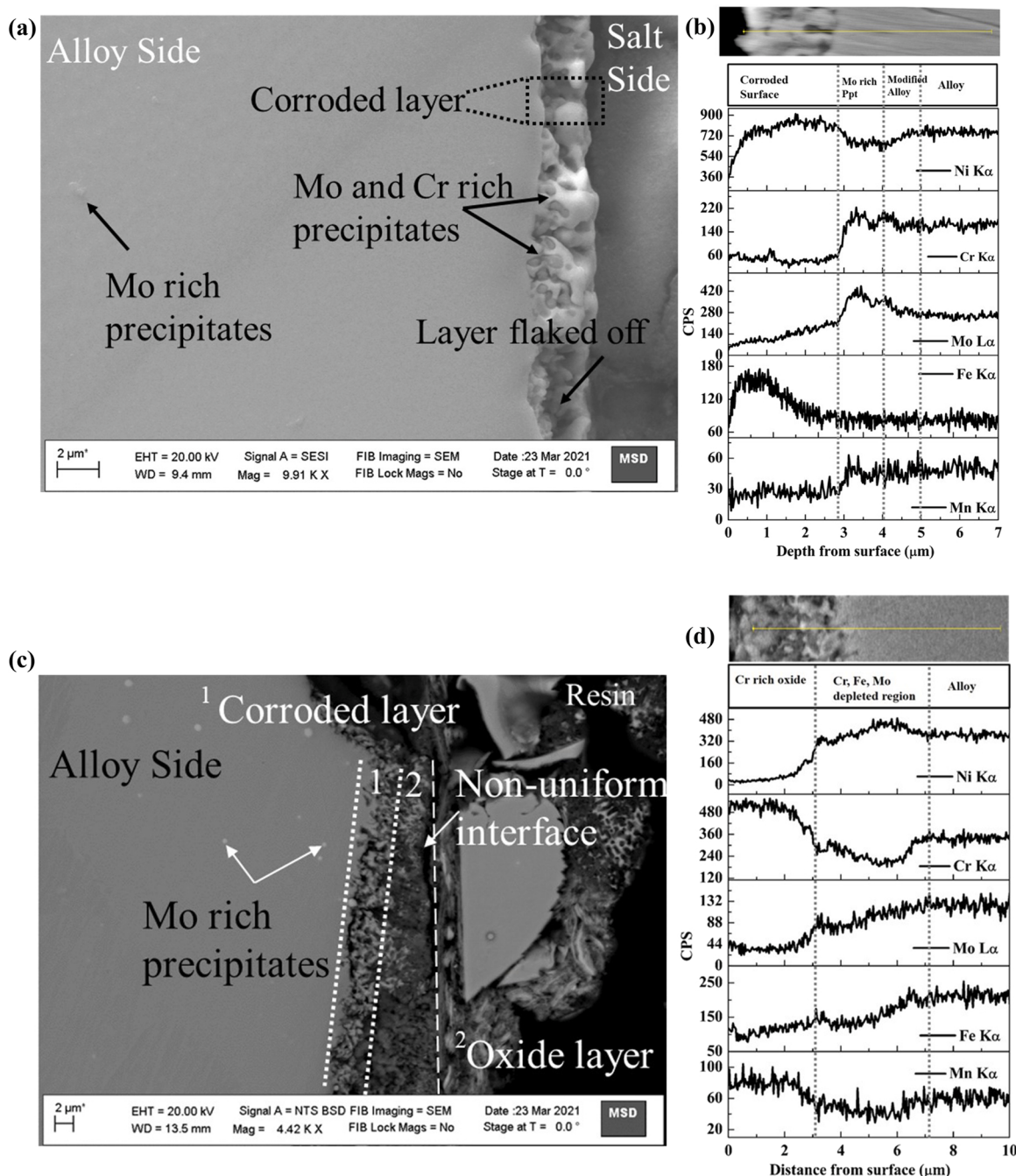


**Fig. 4.** SE image of alloy cross section and corresponding EDS line scan profiles for exposed (a)–(b) Hastelloy N (c)–(d) Hastelloy X.

electron images of the cross-sections of the exposed alloy coupons where the Cr-depleted region is found to be non-uniform. The EDS line profiles for various elements have shown that the Cr-depletion depth extended upto a depth of ~ 2.5–5 μm from the surface in the case of Hastelloy N (Fig. 4(b)) while in the case of Hastelloy X, it extends up to a depth of ~ 4.0–10 μm from the surface (Fig. 4(d)). However, it may be noted that Hastelloy X develops a Cr-rich oxide layer having a thickness ~ 3 μm at the alloy surface. Since the corrosion experiment was carried out in vacuum with very little oxygen or moisture impurity, the formation of Cr layer patches could have occurred when the exposed Hastelloy X specimens when taken out from the experimental set-up into ambient atmosphere.

Another interesting feature observed is the presence of Mo rich phases in the alloy matrices (Fig. 4). In the case of both Hastelloy N and

Hastelloy X, thermal ageing leads to the development of M<sub>6</sub>C type carbides which are exhaustively investigated [31–33]. Moreover, Hastelloy N shows formation of Cr rich precipitates at the alloy/salt interface which could be Cr fluorides (Fig. 5(a)–(b)). However, due to small size of the precipitates, this could not be ascertained from the SEM. Hence, Raman spectroscopic investigations were undertaken. In the case of Hastelloy X, the BSE image for the alloy cross section (Fig. 5(b)) established that areas adjacent to the Mo rich precipitates also suffer from corrosive attack though the precipitates themselves remain intact. Since the ingress of the elements of the salt into the alloy could not be identified under SEM, the alloys were analyzed using SIMS depth profile measurements.

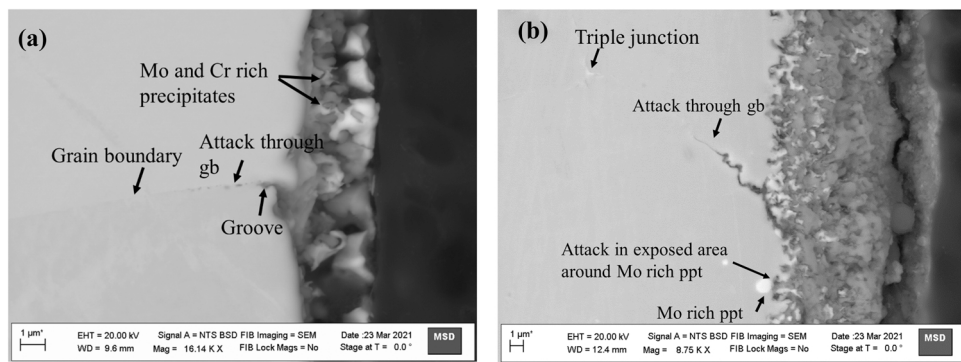


Fig. 5. BSE image of cross section of the exposed coupon of (a) Hastelloy N and (b) Hastelloy X.

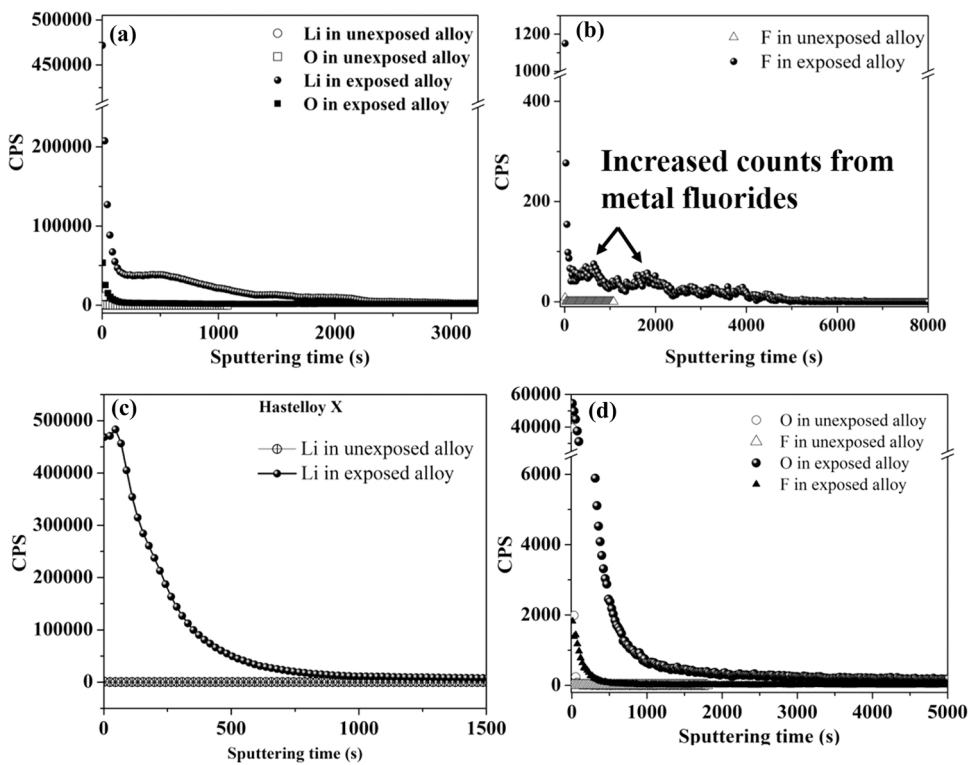


Fig. 6. SIMS depth profiles for the salt elements Li, O and F on the exposed alloy surface (a)-(b) Hastelloy N and (c)-(d) Hastelloy X as a function of sputtering time.

### 3.3. SIMS analysis of exposed alloys

Qualitative SIMS depth profiles for the exposed alloy coupons are shown in Fig. 6. The plots for depth profiles confirm the ingress of Li, Na, K and F into the alloys for both the alloys. SIMS analyses indicate that there is a higher surface penetration of Li as compared to other three elements in the case of the Hastelloy N. Lithium was found to be present even after sputtering for 2500 s while the counts recorded for F, Na and K decreased after ~ 500 s. In the case of Hastelloy X, a similar trend was observed. After sputtering the surface for 500 s, no K, Na and F were detected in the Hastelloy X though the presence of Li in the alloy was detected till a total sputtering time of ~ 1000 s. Additionally increase in the counts for F was observed at multiple sputtering depths for exposed Hastelloy N coupons. This could be attributed to the metal fluorides, possibly the Cr rich precipitates that were observed in the SEM micrographs.

In order to detect the depth of penetration for Li into the alloy, non-contact 3D digital optical profilometry was performed to measure the depth of the craters produced during SIMS sputtering in exposed alloy

coupons (Profilometry images provided in appendix). It was found that the crater depth was around  $7.22 \pm 0.01 \mu\text{m}$  for Hastelloy X and  $4.23 \pm 0.01 \mu\text{m}$  for Hastelloy N. Correlating the crater depth with SIMS data for sputtering time, the sputtering rate of Hastelloy X and Hastelloy N in SIMS depth profiling is estimated to be  $0.500 \pm 0.001 \text{ nm/s}$  and  $0.490 \pm 0.001 \text{ nm/s}$ , respectively. Li is found to be present in the Hastelloy X upto a depth of  $700 \pm 2 \text{ nm}$  and for Hastelloy N upto  $\sim 1500 \text{ nm}$ . Even though the corrosive attack on Hastelloy X is higher than that of Hastelloy N, the Li penetration depth is less. The lower value of the Li depletion depth in Hastelloy X can be attributed to the dissolution of the corroded layer into the FLiNaK salt. In order to investigate the role of Li in any corrosion product formation, Raman spectroscopic investigations at different locations of the exposed alloy surfaces were carried out.

### 3.4. Micro-Raman Spectroscopy

Micro-Raman spectroscopic measurements recorded at different locations on the surfaces of the exposed alloys are presented in Fig. 7. The

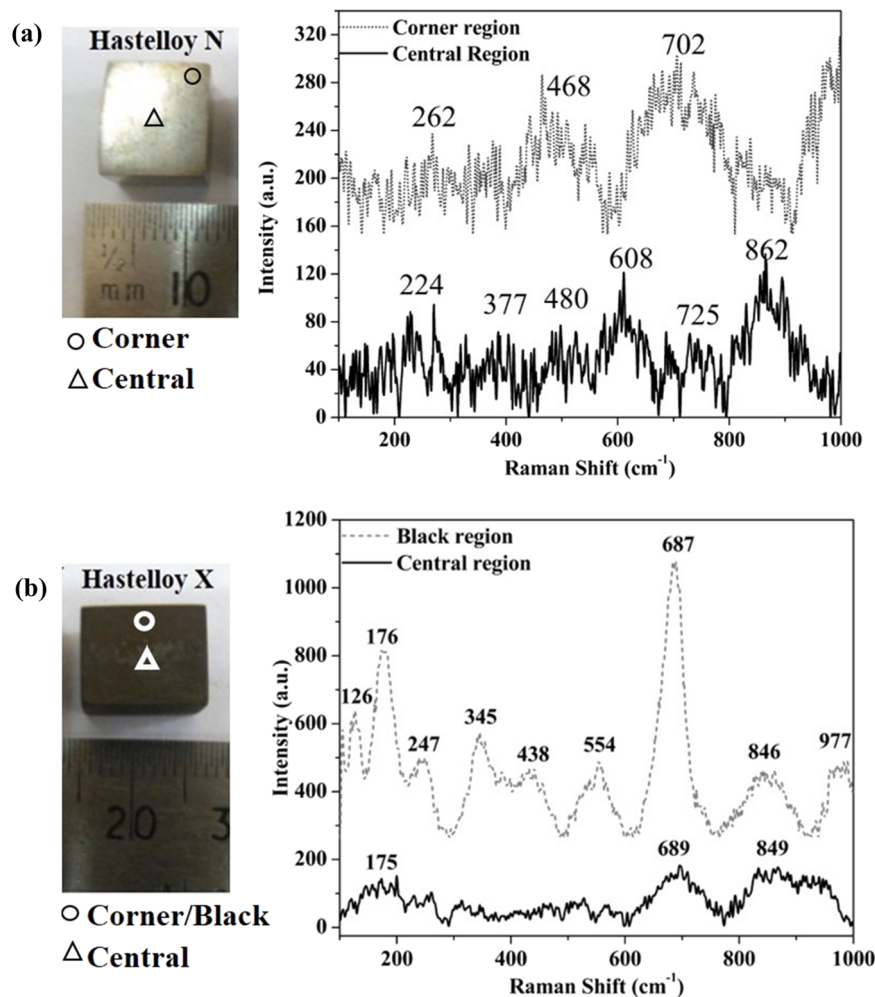


**Fig. 7.** Photograph and Raman spectra for exposed (a) Hastelloy N and (b) Hastelloy X surface.

**Table 7**  
Observed Raman bands in the exposed alloy surface [36–44].

Alloy	Bands observed at (cm⁻¹)	Assigned structure
Hastelloy X- Black region	176,687,438	NiCr <sub>2</sub> O <sub>4</sub> , CoFe <sub>2</sub> O <sub>4</sub>
	345, 554	Cr <sub>2</sub> O <sub>3</sub>
	687	NiFe <sub>x</sub> Cr <sub>2-x</sub> O <sub>4</sub>
	345, 849	LiCr <sub>2</sub> O <sub>4</sub>
	126,977	LiF
Hastelloy X- central region	175,689	NiCr <sub>2</sub> O <sub>4</sub>
	849,	LiCr <sub>2</sub> O <sub>4</sub>
Hastelloy N- Corner region	262,468,702	NiFe <sub>2</sub> O <sub>4</sub>
Hastelloy N- Central region	224	CrF <sub>3</sub>
	377,480,608,725,862	Cr <sub>2</sub> O <sub>3</sub>

Raman bands were identified on the basis of literature inputs [36–40]. From the Raman spectra (Fig. 7), it is evident that the nature of corrosive attack in both the alloys is non-uniform as they show formation of different types of corrosive products at different locations, namely the central location and the corner region. Hastelloy X showed the presence of sharp Raman peaks (Fig. 7(b)) while Hastelloy N showed broad peaks with low intensity (Fig. 7(a)). Raman peak analyses in Hastelloy N indicates the formation of CrF<sub>3</sub> in concordance with previous studies carried out by Ye et al. [21]. Raman bands formed at 377 cm⁻¹ is associated with the symmetric stretching vibrations of fluorine species bonded by the modifying cations [37] which basically is the molten salt ingress in the sample. The Raman bands 480 and 608 cm⁻¹ can be attributed to the asymmetric vibration of Mo-O-Mo and the symmetric

mode of vibration of the bond, respectively [38]. The band at 176, 687 cm⁻¹ is characteristic of the spinel oxide of CoFe<sub>2</sub>O<sub>4</sub> [39].

The Raman bands at 862 cm⁻¹ lies in the region of 850–970 cm⁻¹ which is attributed to Mo-O bonds [40]. The black region of Hastelloy X is observed to develop intermittent Cr<sub>2</sub>O<sub>3</sub> [41] type oxide while both black and central region of Hastelloy X indicate the formation of spinel of type NiFe<sub>x</sub>Cr<sub>2-x</sub>O<sub>4</sub> [42]. Formation of such spinel is frequently observed in Ni-based alloys exposed to halide melt [43,44]. The Raman band at 849 cm⁻¹ in Hastelloy X strongly suggest the formation of Li rich oxide of type LiCr<sub>2</sub>O<sub>4</sub> [45]. The presence of LiCr<sub>2</sub>O<sub>4</sub> in the central region of Hastelloy X which is devoid of the oxide layer indicates that the Li-chromate is formed during the alloy exposure to FLiNaK salt with the oxygen ions or atoms possibly being picked up from the impurities such as sulphate, dissolved oxygen etc. However, no such Li rich precipitates were observed in Hastelloy N. The exact mechanism of the formation of Li-rich precipitate is not yet known and can be investigated in future studies. The various bands identified in Raman analyses are summarized in Table 7.

#### 4. Discussion

The major observations obtained from the microscopic and spectroscopic investigations can be summarized as follows

- The corrosion of alloys in molten salt during the initial stage (exposure time < 400 h) is mainly impurity driven where the most active element at the surface, viz., Cr reacts with the

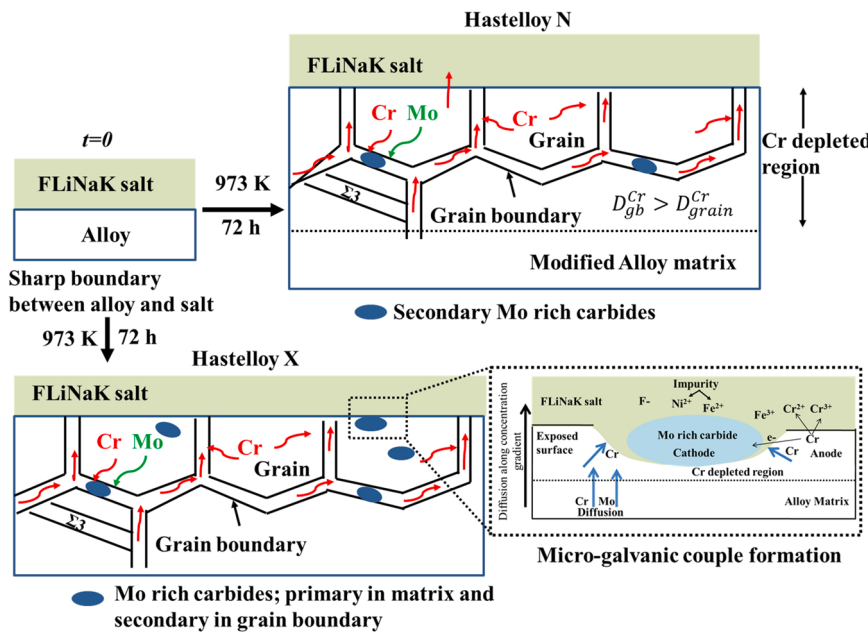


Fig. 8. Schematic showing mechanism of corrosion prevalent in Hastelloy N and Hastelloy X [42].

Table 8

Estimation of Cr diffusivity in the alloys from SEM depletion depth and weigh loss measurements.

Alloy	Cr Depletion depth ( $\mu\text{m}$ )	$D_{\text{Cr, SEM}}$ ( $\text{m}^2/\text{s}$ )	$\Delta w/A$ ( $\text{mg}/\text{cm}^2$ )	$C=C_{\text{Cr,o}} (\text{g}/\text{cc})$	$D_{\text{cr}} = \frac{\pi(\Delta w)^2}{4 * t * c^2} (\text{m}^2/\text{s})$
N	5	$2.41 \times 10^{-17}$	1.044	0.622438	$8.52 \times 10^{-16}$
X	10	$9.64 \times 10^{-17}$	12.917	1.7933	$1.57 \times 10^{-14}$

Table 9

Comparison of the Cr diffusivities in different alloys at 973 K.

Alloy	Cr Diffusivity at 973 K ( $\text{m}^2/\text{s}$ )	Ref
Pure Ni	$2.5 \times 10^{-15}$	22
GH3535	$6.0 \times 10^{-18}$	27
Hastelloy N	$2.81 \times 10^{-16}$ lattice diffusion	21
In FLiNaK salt	$2.48 \times 10^{-15}$ at gb	17

impurities (in this case sulphate, residual moisture and  $\text{FeF}_2$ ) and gets fluorinated.

- (b) The Gibbs free energy for fluoride formation of various Ni, Al, Cr and Mo on the other hand, follows the trend  $\text{AlF}_3 < \text{CrF}_2/\text{CrF}_3 < \text{NiF}_2 < \text{MoF}_2$  and thus mainly Cr rich fluorides are formed at the surface which dissolve into the molten salt. The dissolution of Cr rich fluorides sets up a concentration gradient of Cr across the alloy matrix and surface resulting in more Cr diffusion which ultimately determines the corrosion rate of an alloy in molten salts.
- (c) SIMS analyses revealed that elements of the salt, particularly Li and F, also diffuse into the alloy. Also, fluoride rich precipitates formed at the Hastelloy N/salt interface.

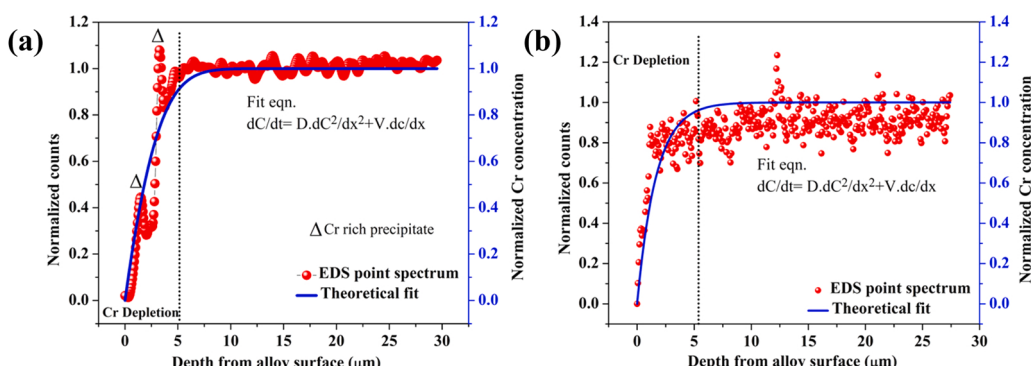


Fig. 9. Modelling the Cr depletion in (a) Hastelloy N and (b) Hastelloy X using modified Fick's law.

#### 4.1. Effect of alloying elements and secondary phase on the dissolution behaviour

The activation energy for diffusion and diffusion coefficient of F in Ni-alloy at 973 K are reported to be 118.6 KJ/mol and  $\sim 4.03 \times 10^{-9}$  cm<sup>2</sup>/s respectively [15,17,48]. Since diffusivity of F ( $10^{-9}$  cm<sup>2</sup>/s) is much higher than the Cr ( $10^{-15}$  cm<sup>2</sup>/s) [14,21–26], the rate is limited by Cr diffusion. Furthermore, the susceptibility of alloy to corrosive attack is given by an index defined as  $W_{\text{Fe}+\text{Cr}}$ , the value of which is higher for the alloy more susceptible to uniform corrosive attack [17]. The value of  $W_{\text{Fe}-\text{Cr}}^{\text{Hastelloy N}}$  is found to be  $11 \pm 0.6$  wt% which is less than that of Hastelloy X  $39.6 \pm 0.7$  wt% indicating the latter is more susceptible to corrosive attack consistent with the observed trend in Cr depletion. As Hastelloy-X is more susceptible to uniform corrosion, higher concentration gradients (dC/dx) and consequently faster Cr diffusion to the surface is expected. This led to enhanced corrosion rates Hastelloy-X, as indicated through higher weight loss and dissolution rates.

Secondary phases present in the alloy also play a role in enhancing/mitigating the corrosion process. Both Hastelloy N and Hastelloy X contain Mo-rich precipitates, Hastelloy X contain primary Mo-rich precipitates and develop secondary Mo-rich precipitates when exposed to elevated temperatures. Similarly, Hastelloy N too develops secondary Mo-rich carbides at the grain boundaries at higher temperature of exposure though the alloy at room temperature is precipitate free. However, the fraction of carbide precipitates is higher for Hastelloy X in comparison to Hastelloy N.

Since Mo is more noble as compared to Cr, the Mo rich carbide performs as cathode and the exposed alloy surface around the carbide precipitate acts as anode thereby forming a micro-galvanic cell. This leads to the corrosive attack around the Mo-rich precipitates causing them to finally drop-off from the matrix and results in pit formation. Similar mechanism was proposed for the depletion of Cr in Cr<sub>23</sub>C<sub>6</sub> type carbides at high angle boundaries by Dai et. al [46]. The proposed mechanism of enhancement in Cr dealloying in presence of carbides is depicted schematically in Fig. 8.

#### 4.2. Modelling Cr depletion

From the characteristic diffusion distance obtained from SEM (Cr depletion depth) for the alloy cross-sections, the effective diffusion co-

$$D_{\text{Cr}} = \frac{\pi}{t} \left( \frac{\Delta M}{2A t C_0} \right)^2 \quad (5)$$

Where the symbols have their usual meanings. The surface concentration of Cr,  $C_0$  is estimated using the relation as follows using the standard density values for elements (Details in appendix)

$$C_0 = \frac{\text{wt.\% of Cr at the alloy surface}}{\sum \left( \frac{\text{wt.\% of individual element at the alloy surface}}{\text{Density of the element}} \right)} \quad (6)$$

The surface concentration is estimated to be  $C_0 = 0.622438$  g/cc for Hastelloy N and  $C_0 = 1.79347$  g/cc for Hastelloy X. The Cr diffusivities a calculated using both the methods are presented in Table 8.

The Cr diffusivity calculated from the SEM depletion depth are one order lower than the values reported in literature. On the other hand, the diffusivity estimated from weight loss is in concordance with the literature reports for Hastelloy N but one order higher for Hastelloy X (Table 9).

The Cr depletion in the Ni-Mo-Cr alloys has been modelled by many researchers using the Fick's law. However, the effect of the dissolving layer at the alloy/salt interface should be incorporated in the Fick's law for the accurate prediction of Cr depletion. Such a formalism has been adapted by Chakraborty et al. [48] to simulate the Cr depletion in RAFMS steel when exposed to Pb-Li eutectic [48]. Hence, the Fick's 2nd law is rewritten incorporating the effect of the dissolution of the interface as [48].

$$\frac{dC}{dt} = D \frac{d^2C}{dx^2} + V \cdot \frac{dC}{dx} \quad (6)$$

Where  $C(x, 0) = C_0$  and  $C(0, t) = 0$ , for  $t > 0$ .  $V$ : dissolution rate of the interface;  $D$  is the Cr diffusivity,  $C(x, t)$ : Cr content as a function of depth in the matrix  $x$ ; and time  $t$ ;  $C_0$  is the initial surface concentration of Cr at  $t = 0$ . Eq. (6) can be resolved with Laplace transforms into Eq. (7).

$$\frac{C(x, t)}{C_0} = 1 - 0.5 \left\{ \operatorname{erfc} \left[ \frac{x + Vt}{2D^{0.5}t^{0.5}} \right] + \exp(-VD^{-1}x) \times \operatorname{erfc} \left[ \frac{x - Vt}{2D^{0.5}t^{0.5}} \right] \right\} \quad (7)$$

Substituting the values as  $t = 2.592 \times 10^5$  s,  $D = D_{\text{Cr}}$ , SEM from Table 9,  $V$  = thickness reduction rate (m/s) from Table 2, the equations are modified respectively for Hastelloy N and Hastelloy X as

$$\frac{C(x, t)}{C_0} = 1 - 0.5 \{ \operatorname{erfc} [0.20047 * (x + 1.1508)] + \exp(-0.185x) \times \operatorname{erfc} [0.20047 * (x - 1.1508)] \} \quad (8)$$

$$\frac{C(x, t)}{C_0} = 1 - 0.5 \{ \operatorname{erfc} [0.100026 * (x + 14.976)] + \exp(-0.59935x) \times \operatorname{erfc} [0.100026 * (x - 14.976)] \} \quad (9)$$

efficient of diffusion for Cr can be estimated using relation [47].

$$x = 2(D_{\text{Cr}, \text{SEM}} t)^{1/2} \quad (4)$$

where  $x$  is the depth of Cr depletion known as characteristic diffusion distance and  $t$  is the exposure time. Table 8 shows the Cr diffusivities in both the alloys calculated from the maximum Cr depletion depth. The values obtained are two orders lower than those reported in literature [17,48]. The metal fluorides formed at the surface dissolve back into the molten salt thereby moving the salt-alloy interface inwards with time. Hence the diffusion coefficient estimated using the above equation is underestimated. The upper limit value of Cr diffusivity can be determined from the mass loss measurements which includes the effect of dissolved interface. The diffusivity in this case is obtained by equation [27].

The modelled Cr depletion as a function of depth from the surface of the alloys are presented in Fig. 9 and are found to be in good agreement with the experimentally observed SEM depth profiles.

#### 5. Conclusions

The major findings of the investigation on Hastelloy X and Hastelloy N having varying Mo/Cr ratio exposed to high temperature fluoride melt is summarized below

- (i) The corrosive attack in both the alloys is non-uniform and is accompanied by extensive pitting within the grains as well as in the grain boundary. However, the alloy having higher Cr content or lower Mo/Cr is more susceptible to the corrosive attack.

- (ii) Presence of secondary phases such as Mo-rich carbide was found to be detrimental since these acts as localized cathode for the carbide/alloy micro-galvanic cell and cause higher dissolution in the adjacent region of the exposed alloy.
- (iii) Hastelloy X having lower Mo/Cr ratio has a higher carbide fraction than Hastelloy N and hence undergoes more severe corrosive attack.
- (iv) SIMS study unequivocally establishes that in addition to F, Li also diffuses into the alloy during FLiNaK exposure. Furthermore, in case of Hastelloy X, Li is found to interact with Cr to form precipitates of type  $\text{LiCr}_2\text{O}_4$ .
- (v) The Cr depletion in the alloys was theoretically modelled using modified Fick's law. The predicted result was found to be in good agreement with the experimental measurements.

### CRediT authorship contribution statement

**Rumu H Banerjee:** Conceptualization, Methodology, Investigation, Writing – original draft, **V. Singh:** SEM, Investigation, **P. Chakraborty:** Corrosion facility **V. Karki:** SIMS Investigation, **G. Abraham:** Raman Spectroscopic investigation, Writing – review & editing **R. Tewari:** Writing – review & editing, Supervision.

### Declaration of Competing Interest

The authors declare that they have no known competing financial interests or personal relationships that could have appeared to influence the work reported in this paper.

### Data Availability

The authors do not have permission to share data.

### Acknowledgements

The present study was funded by Department of Atomic Energy, Government of India. The authors thank Dr. Vivekanand Kain, Director, Materials Group for his keen interest in this study. The authors are thankful to Smt. Amrita, MP&CED, BARC for the profilometry measurements.

### Appendix A. Supporting information

Supplementary data associated with this article can be found in the online version at [doi:10.1016/j.corsci.2022.110929](https://doi.org/10.1016/j.corsci.2022.110929).

### References

- [1] J. Serp, M. Allibert, O. Beneš, S. Delpech, O. Feynberg, V. Ghetta, D. Heuer, D. Holcomb, V. Ignatiev, J.L. Kloosterman, L. Luzzi, E. Merle-Lucotte, J. Uhlíř, R. Yoshioka, D. Zhimin, The molten salt reactor (MSR) in generation IV: overview and perspectives, *Prog. Nucl. Energy* 77 (2014) 308–319.
- [2] Molten salt reactors and thorium energy, by Thomas J. Dolan, Woodhead Publishing, Cambridge, USA, 2017.
- [3] T. Allen, J. Busby, M. Meyer, D. Petti, Materials challenges for nuclear systems, *Mater. Today* 13 (12) (2010) 14–23.
- [4] I. Pioro, Handbook of Generation IV Reactors, Woodhead Publishing, Cambridge, USA, 2016.
- [5] V. Dulera, R.K. Sinha, A. Rama Rao, R.J. Patel, Progress in Nuclear Energy, 2017, 101(A), 82–99.
- [6] P.K. Vijayan, A. Basak, I.V. Dulera, K.K. Vaze, S. Basu, R.K. Sinha, Conceptual design of Indian molten salt breeder reactor, *Pramana J. Phys.* 85 (2015) 539–554.
- [7] A.E. Danon, O. Muránsky, I. Karatchevtseva, Z. Zhang, Z.J. Li, N. Scales, J.J. Krizic, L. Edwards, Molten salt corrosion (FLiNaK) of a Ni–Mo–Cr alloy and its welds for application in energy-generation and energy-storage systems, *Corros. Sci.* 164 (2020), 108306.
- [8] O. Muránsky, C. Yang, H. Zhu, I. Karatchevtseva, P. Sláma, Z. Nový, L. Edwards, Molten salt corrosion of Ni–Mo–Cr candidate structural materials for Molten Salt Reactor (MSR) systems, *Corros. Sci.* 159 (2019) 10808.
- [9] L. Jiang, K. Wang, B. Leng, X.X. Ye, S.J. Chen, R.D. Liu, J.P. Liang, C.W. Li, Z.J. Li, Tellurium segregation-induced intergranular corrosion of GH3535 alloys in molten salt, *Corros. Sci.* 194 (2022), 109944.
- [10] I. Victor, S. Aleksandr, Voltammetric measurements on the [U(IV)]/[U(III)] couple and embrittlement of high nickel alloys in fuel LiF-BeF<sub>2</sub>-UF<sub>4</sub> salt with tellurium addition in application to molten salt reactor, *Corros. Sci.* 160 (2019), 108164.
- [11] L. Jiang, W. Wang, X.X. Ye, C.W. Li, J.P. Liang, D.J. Wang, Z.J. Li, Unexpected effect of hydroxyl radical on tellurium corrosion of the Ni–Mo–Cr–Nb based alloy, *Corros. Sci.* 173 (2020), 108748.
- [12] L. Jiang, C.T. Fu, B. Leng, Y.Y. Jia, X.X. Ye, W.Z. Zhang, Q. Bai, S. Xia, Z.J. Li, F. Liu, X.T. Zhou, Influence of grain size on tellurium corrosion behaviors of GH3535 alloy, *Corros. Sci.* 148 (2019) 110–122.
- [13] K.L. Murty, I. Charit, Structural materials for Gen-IV nuclear reactors: Challenges and opportunities, Proceedings of the International Conference on Advances in Nuclear Materials: Processing, Performance and Phenomena, *J. Nucl. Mater.* 383 (2008) 189–195.
- [14] G.S. Was, T.R. Allen, Corrosion Issues in Current and Next-Generation Nuclear Reactors. Structural Alloys for Nuclear Energy Applications, Elsevier, Cambridge, MA, 2019, pp. 211–246.
- [15] S.Q. Guo, J.S. Zhang, W. Wu, W.T. Zhou, Corrosion in the molten fluoride and chloride salts and materials development for nuclear applications, *Prog. Mater. Sci.* 97 (2018) 448–487.
- [16] M. Wang, Q. Nai, J. Qiu, B. Wang, C. Yang, C. Su, J. Liang, Development of GH3535 alloy for thorium molten salt reactor, in: Y. Han (Ed.), *Advances in Energy and Environmental Materials*, Springer, Singapore, Singapore, 2018, pp. 137–147.
- [17] R.H. Banerjee, Vishal Singh, A. Arya, S. Banerjee, A comparative study of surface layer formation in Ni-based alloys with varying Cr contents exposed to high temperature fluoride environment, *J. Nucl. Mater.* 516 (2019) 54–62.
- [18] R.H. Banerjee, A. Arya, H. Donthula, C. Nayak, D. Bhattacharya, S. Banerjee, Quantitative description of the role of Cr on the ordering characteristics of a single phase Ni-16 wt% Mo- 7wt% Cr alloy, *Acta Mater.* 219 (2021), 117263.
- [19] P. Chakraborty, R.H. Banerjee, N. Keskar, R. Tewari, V. Kain, Facility to test the compatibility of materials in molten salts for MSBR applications, BARC Newsletter, Apr 2021, ([http://www.barc.gov.in/barc\\_nl/2021/2021030401.pdf](http://www.barc.gov.in/barc_nl/2021/2021030401.pdf)).
- [20] S. Delpech, C. Cabet, C. Slim, G.S. Picard, Molten fluorides for nuclear applications, *Mater. Today* 13 (2010) 34–41.
- [21] X. Ye, H. Ai, Z. Guo, H. Huang, L. Jiang, J. Wang, Z. Li, X. Zhou, The high temperature corrosion of Hastelloy N alloy (UNS N 10003) in molten fluoride salts analysed by STXM, XAS, XRD, SEM, EPMA, TEM/EDS, *Corros. Sci.* 106 (2016) 249–259.
- [22] F.Y. Ouyang, C.H. Chang, B. Yu, T.K. Yeh, J.J. Kai, Effect of moisture on corrosion of Ni-based alloys in molten alkali fluoride FLiNaK salt environments, *J. Nucl. Mater.* 437 (2013) 201–207.
- [23] H. Yin, J. Qiu, H. Liu, W. Liu, Y. Wang, Z. Fei, S. Zhao, X. An, J. Cheng, T. Chen, P. Zhang, G. Yu, L. Xie, Effect of CrF<sub>3</sub> on the corrosion behaviour of Hastelloy-N and 316 L stainless steel alloys in FLiNaK molten salt, *Corros. Sci.* 131 (2018) 355–364.
- [24] M. Lee, O. Muránsky, I. Karatchevtseva, H. Huang, K.J. Laws, Corrosion performance of Ni-based structural alloys for applications in molten-salt based energy systems: Experiment & numerical validation, *Corros. Sci.* 90 (2021), 109607.
- [25] Y. Jia, F. Han, Z. Li, R. Liu, B. Leng, X. Li, Y. Lu, X. Zhou, Effect of  $\text{SO}_4^{2-}$  ion impurity on stress corrosion behavior of Ni-16Mo-7Cr alloy in FLiNaK salt, *J. Nucl. Mater.* 547 (2021), 152809.
- [26] H. Ai, Y. Liu, M. Shen, H. Liu, Y. Chen, X. Yang, H. Liu, Y. Qian, J. Wang, Dissolved valence state of iron fluorides and their effect on Ni-based alloy in FLiNaK salt, *Corros. Sci.* 192 (2021), 109794.
- [27] O. Muránsky, I. Karatchevtseva, A.E. Danon, R. Holmes, P. Huai, Z. Zhang, Impact of dislocations and dislocation substructures on molten salt corrosion of alloys under plasticity-imparting conditions, *Corros. Sci.* 176 (2020), 108915.
- [28] Y. Wang, K. Sridharan, A. Couet, Method for identification of redox control parameters for corrosion mitigation in molten fluoride salts, *J. Nucl. Mater.* 543 (2021), 152624.
- [29] V. Pavlik, M. Boča, A. Kityk, Accelerated corrosion testing in molten fluoride salts: effect of additives and the crucible material, *Corros. Sci.* 195 (2022), 110011.
- [30] L.C. Olson, J.W. Ambrosek, K. Sridharan, M.H. Anderson, T.R. Allen, Materials corrosion in molten LiF-NaF-KF salt, *J. Fluor. Chem.* 130 (1) (2009) 67–73.
- [31] J.M. Leitnaker, G.A. Potter, D.J. Bradley, J.C. Franklin, W.R. Laing, The composition of eta carbide in Hastelloy N after aging 10,000h at 815°C, *Metall. Trans. A* 9 (1978) 397–400.
- [32] Z. Xu, L. Jiang, J. Dong, Z. Li, X. Zhou, The effect of silicon on precipitation and decomposition behaviours of  $\text{M}_6\text{C}$  carbide in a Ni–Mo–Cr superalloy, *J. Alloy. Comp.* 620 (2015) 197–203.
- [33] R. Gehlbach, H. McCoy Jr., Phase instability in Hastelloy N in: International Symposium on Structural Stability in Superalloys, Seven Springs, Pennsylvania, 1968, 346–366.
- [34] F. Han, L. Jiang, X. Ye, Y. Lu, Z. Li, X. Zhou, Carbides evolution in a Ni-16Mo-7Cr base superalloy during long-term thermal exposure, *Materials* 521 (2017) 1–7.

- [35] Y. Han, X. Xue, T. Zhang, R. Hu, J. Li, Grain boundary character correlated carbide precipitation and mechanical properties of Ni-20Cr-18W-1Mo superalloy, Mater. Sci. Eng. A 667 (2016) 391–401.
- [36] P. Daniel, A. Bulou, M. Rousseau, J. Nouet, M. Leblanc, Raman-scattering study of crystallized MF<sub>3</sub> compounds (M = Al, Cr, Ga, V, Fe, In): An approach to the short-range-order force constants, Phys. Rev. B 42 (1990) 545–552.
- [37] L.F. Santos, R.M. Aldeida, V.K. Tikhomirov, A. Jha, J. Non Cryst. Solids, 2001, 284, 43.
- [38] A.M. Milankovic, A. Santic, A. Gajovic, D.E. Day, J. Non Cryst. Solids, 2003, 325, 76.
- [39] G.V.M. Jacintho, A.G. Brolo, P. Corio, P.A.Z. Suarez, J.C. Rubim, Structural investigation of MFe<sub>2</sub>O<sub>4</sub> (M ¼ Fe, Co) magnetic fluids, J. Phys. Chem. C. 113 (2009) 7684–7691.
- [40] L. Koudelka, I. Rösslerová, J. Holubová, P. Mošner, L. Montagne, B. Revel, J. Non-Cryst. Solids, 2011, 357, 2816.
- [41] A.R. Shankar, A. Kanagasundar, U. Kamachi Mudali, Corrosion of nickel-containing alloys in molten LiCl-KCl medium, Corrosion 69 (2013) 48–57.
- [42] Z. Wang, S.K. Saxena, P. Lazor, H.S.C. O'Neill, An in-situ Raman spectroscopic study of pressure induced dissociation of spinel NiCr<sub>2</sub>O<sub>4</sub>, J. Phys. Chem. Solids 64 (2003) 425–431.
- [43] J. Ch, Rao, S. Ningshen, High temperature molten salt corrosion of structural materials in UCl<sub>3</sub>-LiCl-KCl, Corros. Eng. Sci. Technol. (2020), <https://doi.org/10.1080/1478422X.2020.1741869>.
- [44] W. Phillips, D. Chidambaram, Effect of metallic Li on the surface chemistry of inconel 625 exposed to molten LiCl-Li<sub>2</sub>O, J. Electrochem. Soc. 166 (2019) C3193.
- [45] H. Zou, X. Liang, X. Feng, H. Xiang, Chromium-modified Li<sub>4</sub>Ti<sub>5</sub>O<sub>12</sub> with a synergistic effect of bulk doping, surface coating, and size reducing, ACS Appl. Mater. Interfaces 8 (2016) 21407–21416.
- [46] Q. Dai, X. Xi Ye, H. Ai, S. Chen, L. Jiang, J. Liang, K. Yu, B. Leng, Z. Li, X. Zhou, Corrosion of Incoloy 800H alloys with nickel cladding in FLiNaK salts at 850 °C, Corros. Sci. 133 (2018) 349–357, <https://doi.org/10.1016/j.corsci.2018.01.026>.
- [47] P. Shewmon, Diffusion in Solids, Springer Nature, Switzerland, 2016.
- [48] P. Chakraborty, V. Singh, S. Bysakh, R. Tewari, V. Kain, Short-term corrosion behavior of Indian RAFM steel in liquid Pb-Li: corrosion mechanism and effect of alloying elements, J. Nucl. Mater. 520 (2019) 208–217.